Catalysis Letters
https://doi.org/10.1007/s10562-019-02975-5

Iron Oxide as a Promoter for Toluene Catalytic Oxidation Over Fe–Mn/γ-Al_2O_3 Catalysts

Linbo Qin[1,2] · Xinming Huang[1,2] · Bo Zhao[1,2] · Yu Wang[1,2] · Jun Han[1,2]

Received: 12 August 2019 / Accepted: 17 September 2019
© Springer Science+Business Media, LLC, part of Springer Nature 2019

Abstract

Fe–Mn/γ-Al_2O_3 catalysts that prepared by the wet-impregnation method were used to degrade toluene, a VOCs model compound. The results indicated that the 10Fe–15Mn/γ-Al_2O_3 exhibited 95% of toluene conversion as well as 95% of CO_2 yield at 300 °C. The Fe–Mn/γ-Al_2O_3 showed a better toluene oxidation activity with respect to the Fe/γ-Al_2O_3 and Mn/γ-Al_2O_3. The introduction of Fe into the Mn/γ-Al_2O_3 resulted in higher surface area, higher $Mn^{3+}/(Mn^{3+}+Mn^{4+})$ ratio, lower reduction temperature, and homogenous distribution of Mn. Meanwhile, the co-exist of the Fe^{3+} and Mn^{3+} over the 10Fe–15Mn/γ-Al_2O_3 also favored for the oxygen transfer, which may enhance the catalytic oxidation performance. The initial toluene was adsorbed on surface of the catalysts and formed benzoyl oxide (C_6H_5–CH_2–O), and then the benzoyl oxide (C_6H_5–CH_2–O) was oxidized to benzaldehyde. Furthermore, the benzaldehyde was further oxidized to form benzoic acid that could be converted to CO_2 and H_2O.

Electronic supplementary material The online version of this article (https://doi.org/10.1007/s10562-019-02975-5) contains supplementary material, which is available to authorized users.

✉ Bo Zhao
zhaobo87@wust.edu.cn

✉ Jun Han
hanjun@wust.edu.cn

[1] Hubei Key Laboratory for Efficient Utilization and Agglomeration of Metallurgic Mineral Resources, Wuhan University of Science and Technology, Wuhan 430081, People's Republic of China

[2] Hubei Provincial Industrial Safety Engineering Technology Research Center, Wuhan University of Science and Technology, Wuhan 430081, People's Republic of China

Published online: 30 September 2019

Graphic Abstract

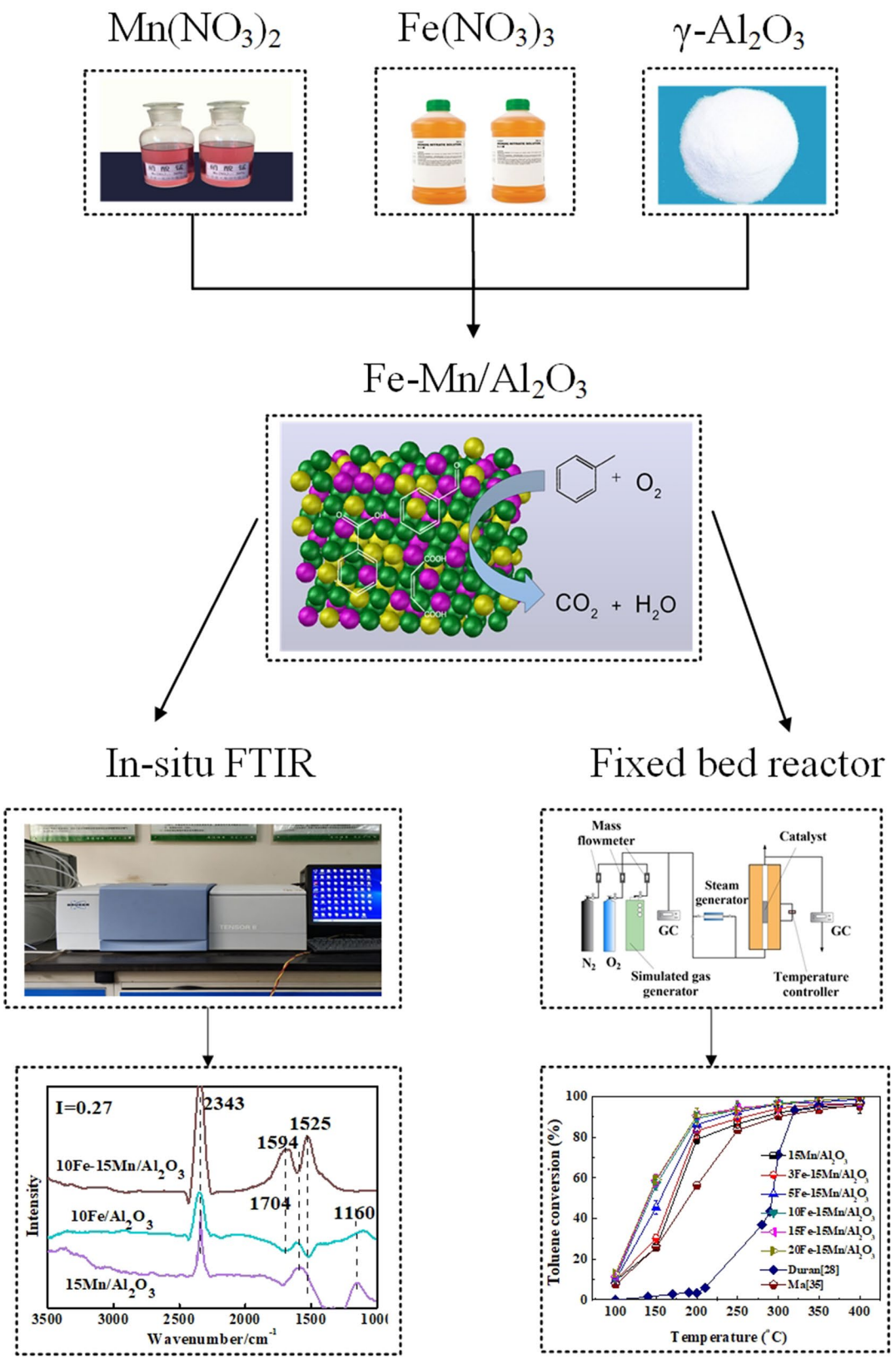

Keywords Fe–Mn/γ-Al_2O_3 · In-situ FTIR · Iron oxide · Toluene oxidation

1 Introduction

Volatile organic compounds (VOCs) are regarded as a contributor of photochemical smog, global warming, and ozone depletion [1–3]. Over 300 VOCs has been recognized as the major contributors to air pollution by U.S. Environmental Protection Agency. Among them, the aromatic VOCs including benzene, toluene, o-xylene, chlorobenzene and etc., with high toxicity to human health and "carcinogenic-mutagenic-teratogenic" effect, mainly originate from industrial source [4]. It was estimated that China emits 31.12 million tons of VOCs in 2015 [5]. The industrial sources VOCs contribute to over 50% of the total emissions [6–8]. In order to reduce VOCs emissions, VOCs has been regarded as one of the main air pollutants by Chinese government in 2010. In 2015, it was proposed that reducing 10% of VOCs emissions from the typical regions and industries compared to those in 2015 during the Chinese 13th Five-Year Plan.

At present, several technologies including adsorption [9], catalytic oxidation [10], thermal oxidation [11–14], plasma oxidation [15], photocatalysis [16], and biotechnology [5] are used to control the VOCs emission. Among these technologies, catalytic oxidation is regarded as one of the most effective method for removing VOCs with producing CO_2 and H_2O at 250–550 °C [17]. In catalytic reaction system, there are two types of catalysts that are widely used for VOCs degradation. One is supported precious metals catalysts such as Au, Ag, and Pt, which shows higher low-temperature catalytic performance, while their applications are limited due to its high cost, and easily poisoning [18]. Another is the transition-metal oxide catalysts, including Fe, Mn, Cu, Ni, and Co, that have advantages of low cost and easy availability compared to the supported precious metal [19]. Manganese oxide (MnO_x) is one of the transition metal oxides that widely used for catalytic oxidation of gaseous pollutants (CO, NO and VOCs) since it is characterized with varied valences of Mn (viz. Mn^{2+}, Mn^{3+} and Mn^{4+}), low cost, and environmental friendliness [20]. Nevertheless, the catalytic performance of the individual MnO_x in terms of stability and activity is not satisfied with the requirement for aromatic VOCs degradation [21].

The introduction of Fe, Cu, Ce, and Co into Mn-based oxides is one of the major methods for improving the catalytic activities. Chen [4] reported that a homogenous $3MnO_x$–$1CeO_y$ (3Mn1Ce) prepared by hydrolysis driving redox method exhibits a higher toluene oxidation performance compared to MnO_2 and CeO_2, which was also proved by Du [22]. Zhang [23] claimed that 90% of benzene conversion is obtained at 191 °C for the nanosheet Co–Mn oxides under the conditions of 20,000 ml g^{-1} h^{-1} and 1500 ppm of benzene. Wang [24] found that the layered Cu–Mn oxide exhibited good catalytic activity for VOCs oxidation due to the formation of Cu^{2+}–O^{2-}–Mn^{4+}, resulting in more active oxygen and vacancies species in Cu–Mn oxide, which was also proved by Hu [25]. Fe-based oxides used as a promoter to synthetize multi-metal catalysts have received widely attention due to its low cost, good stability and higher moisture toleration [26]. Baldi [27] also observed a similar catalytic performance of Mn_2O_3–Fe_2O_3 prepared by co-precipitation with respect to Mn_2O_3. Durán [28] found that the mechanical mixture of Mn_2O_3 and Fe_2O_3 exhibited a catalytic activity similar to those of Mn_2O_3, but the catalytic oxidation activities of representative VOCs over Fe–Mn mixed oxides prepared using the citrate method was higher than that of the Fe_2O_3 and Mn_2O_3, indicating that synergy effects between Fe and Mn were benefitable for enhancing the catalytic performance. Quiroga [29] also found that Fe–Mn mixed oxides catalyst synthetized by mechano-chemical reaction exhibits higher n-hexane oxidation activity compared to Fe_2O_3 and MnOx. Chen [17] reported that Fe–Mn binary oxides synthetized via hydrolysis driving redox method shows higher toluene oxidation activity compared to MnOx. However, the low cost methods for preparing Fe–Mn oxides catalyst (mainly include mechanical mixture, impregnation, and co-precipitation) are difficult to obtain homogeneous oxide, which results in lower catalytic oxidation performance for VOCs [30]. Meanwhile, these Fe–Mn oxides catalysts prepared by Durán [28], Quiroga [29] and Chen [17] showed deactivation towards VOC degradation.

Previous investigations had reported that the metal oxides loaded on supports shows higher catalytic activity and homogenous distribution of active components than the unsupported metal oxide catalyst due to the synergy effects between supports and active component [31]. Metal oxide loaded on supports such as α-Al_2O_3 and γ-Al_2O_3, SiO_2, TiO_2, ZrO_2, cordierite and attapulgite have been received wide investigation [31–33]. Wang [34] found that Cu–Mn/γ-Al_2O_3 showed a better toluene catalytic activity than CuO–MnOx due to homogenous distributions of Mn and Cu into the γ-Al_2O_3. Ma [35] reported that the Fe–Mn/cordierite exhibited higher toluene catalytic activity compared to the unsupported Fe–Mn mixed oxides. At present, Fe–Mn/Al_2O_3 has been widely investigated for NO and mercury oxidation since it is characterized with higher catalytic activity, good stability and higher moisture toleration [36, 37]. However, Fe–Mn oxides loaded Al_2O_3 (Fe–Mn/Al_2O_3) has not been developed for VOCs removal.

In this paper, a series of Fe–Mn/γ-Al_2O_3 catalysts are synthetized using wet-impregnation method, and the catalytic oxidation of toluene over the Fe–Mn/γ-Al_2O_3 catalysts are also evaluated. Meanwhile, these catalysts are also

characterized by means of the BET, XRD, XPS, H_2-TPR, and in situ FTIR.

2 Experimental

2.1 Catalysts Preparation

A series of xFe–yMn/γ-Al_2O_3 catalysts were prepared by the wet-impregnation method. In briefly, γ-aluminum oxide (γ-Al_2O_3, 100–200 μm) was used as the support. Iron (III) nitrate ($Fe(NO_3)_3$, 20 wt% aqueous solution) and manganese(II) nitrate ($Mn(NO_3)_2$, 20 wt% aqueous solution) were used as active components. γ-Al_2O_3 was added into the solutions that prepared from the stoichiometric amount of $Fe(NO_3)_3$, $Mn(NO_3)_2$ and double distilled water, and then stirred at 30 °C for 6 h. Afterward, the samples were washed and dried at 105 °C for 4 h, and then calcined at 400 °C for 4 h. These catalysts obtained from the wet-impregnation of $Fe(NO_3)_3$ and $Mn(NO_3)_2$ with γ-Al_2O_3 support were denoted as xFe–yMn/γ-Al_2O_3, where x and y represented the weight percentage of Fe_2O_3 and MnO_2 based on the γ-Al_2O_3 support, e.g. 10Fe–15Mn/γ-Al_2O_3.

2.2 Catalysts Characterization

In this study, an automated adsorption analyzer (BET, Micromeritics ASAP 2020) was used to analyze the BET surface, pore volume and pore size distribution of these xFe–yMn/γ-Al_2O_3 catalysts. X-ray diffractometer (XRD, Rigaku Dmax/2400) was employed to characterize the crystalline structures of these catalysts. X-ray photoelectron spectroscopy (XPS, AXIS ULTRADLD) was used to measure the compositions of the catalysts. Meanwhile, the contents of Fe and Mn in these catalysts were also measured by the inductively coupled plasma-mass spectrometry (ICP-MS, ELAN DRC-e).

In addition, temperature-programmed reduction (H_2-TPR) were tested on a micromeritics Chem star™ (Quanta chrome Instruments). The catalysts were firstly pretreated in argon (Ar) atmosphere at 300 °C for 60 min, and then the temperature was increased to 1000 °C under a heating rate of 10 °C min^{-1} with a flow rate of H_2/Ar (H_2/Ar ratio is 10: 90) of 20 ml min^{-1}, and the H_2 consumption is continuously recorded.

2.3 In Situ DRIFTS Test

In-situ FTIR experiments were carried out on an FTIR spectrometer (FTIR, Bruker Tensor II) equipped with a Harrick reaction cell under the wavenumber range of 4000–1000 cm^{-1}. Before the experiment, 20 mg catalyst loaded in Harrick reaction cell was pretreated at 300 °C in a Ar atmosphere for 0.5 h and then cooled to 50 °C under Ar atmosphere. To evaluate the effect of reaction temperature, the simulated gas containing about 400 mg m^{-3} toluene was introduced to the Harrick reaction cell under a flow rate of 20 ml min^{-1} (Ar or Ar + O_2), and then the FTIR spectra were continuously recorded as the reaction temperature was heated from 50 to 400 °C with the heating rate of 10 °C min^{-1}.

2.4 Catalytic Test

The catalytic test was performed in a fixed reactor, which consisted of a gas supply device, a reactor and gas measuring system, as detail described in our previous paper [38, 39]. The reactor had a length of 1000 mm and an internal diameter of 20 mm. The simulated gases were provided by gas cylinders controlled by mass flow meters. The H_2O vapor was provided using a water saturator coupled with a U-type absorption tube, and the toluene was supplied by an injection pump and an evaporator (FD-PG, Suzhou, China). The simulated gas contains 400 ± 10 mg m^{-3} of toluene. The gas measuring system consisted of a gas chromatography equipped with a flame ionization detector (FID) and a thermal conductivity detector (TCD) (GC, Agilent 7820A), and gas chromatography–mass spectrometry (GC/MS, QP2010 SE). To evaluate the oxidation activity of these catalysts at 100–400 °C, the catalytic oxidation of toluene was tested in a fixed bed reactor packed with 4.0 g of catalysts (100–200 μm) under gas hourly space velocity (GHSV) range of 20,000 h^{-1}. When the effects of different GHSV and oxygen content were evaluated for the oxidation activity of these catalysts, the flow rates of O_2 and N_2 were adjusted to satisfy with the requirements of GHSV and O_2 content. To investigate the effect of H_2O on the oxidation activity of these catalysts, 10 vol% H_2O was introduced into the simulated gas. The composition of the outlet gas was on-line monitored by the GC and GC/MS. The toluene conversion was calculated by the difference of the toluene concentration. CO_2 in the outlet gas was also detected by GC–TCD, and the rare content of other byproducts in exhaust gas were also recorded by the GC/MS. The toluene conversion and CO_2 yields were calculated according to the Eqs. (1) and (2):

$$X_T = \frac{C_{\text{in}}^{\text{Toluene}} - C_{out}^{Toluene}}{C_{in}^{Toluene}} \times 100\% \tag{1}$$

$$X_{CO_2} = \frac{C_{out}^{CO_2}}{7 \times \left(C_{in}^{Toluene} - C_{out}^{Toluene}\right)} \times 100\% \tag{2}$$

where X_T was the toluene conversion (%); X_{CO_2} was the CO_2 yields (%); while $C_{in}^{Toluene}$ and $C_{out}^{Toluene}$ were the concentration of toluene in the inlet and outlet gas, respectively; $C_{out}^{CO_2}$ was the concentration of CO_2 in the outlet gas.

3 Results and Discussion

3.1 Catalyst Characterization

3.1.1 BET

The pore properties of these Fe–Mn/γ-Al_2O_3 catalysts were summarized in Table 1, it can be seen that the pore properties of the γ-Al_2O_3 such as BET surface area, pore volume and pore diameter were in sequence as 136 ± 9 m^2 g^{-1}, 0.194 ± 0.016 cm^3 g^{-1} and 56.75 ± 1.23 nm. After doping with Fe_2O_3 or MnO_2, the BET surface areas of Mn/γ-Al_2O_3 or Fe/γ-Al_2O_3 catalysts were obviously reduced, while the pore volume and pore diameter of the Mn/γ-Al_2O_3 or Fe/γ-Al_2O_3 catalysts were slightly increased. As the weight fraction of MnO_2 was added from 0 to 20%, the BET surface areas of xMn/γ-Al_2O_3 were gradually decreased from 136 ± 9 to 88 ± 3 m^2 g^{-1}. The pore volumes of the xMn/γ-Al_2O_3 have the similar values at 0.224–0.225 cm^3 g^{-1} when the MnO_2-doping was range of 3–10%, while the pore volumes of the xMn/γ-Al_2O_3 were gradually decreased as the the MnO_2-doping was increased from 10 to 20%. As for the pore diameter, the pore diameter of the xMn/γ-Al_2O_3 were firstly increased and then decreased as the weight fraction of MnO_2 was added from 0 to 20%, and the maximum pore diameter (76.78 nm) were obtained for the 15Mn/γ-Al_2O_3. For the 10Fe–15Mn/γ-Al_2O_3 catalyst, the BET surface area was increased, while the pore volume and pore diameter was decreased compared with the 15Mn/γ-Al_2O_3 catalyst. These results indicated that the role of Fe doping was likely to enhance the homogeneous distribution of Mn on the γ-Al_2O_3, which may benefit for increasing the BET surface of the catalyst [37]. This was also confirmed by the XRD.

3.1.2 XRD

Figure 1 presented the crystalline structures of these catalysts. There were several peaks corresponding to the γ-Al_2O_3 at 37.4°, 45.8°, 64.9°, and 66.9° observed on the surface of these catalysis (JCPDS NO. 35-0121) [37]. Several diffraction peaks located at 23.1°, 32.8°, 38.2°, 45.4°, 49.3°, 55.3°, 61.0°, 64.1° and 65.8° detected, which were attributed to Mn_2O_3 (JCPDS NO. 89-4836), were gradually increased as the weight fraction of Mn increase. Meanwhile, the characteristic peaks (24.2°, 33.1°, 35.7°, 41.0°, 49.2°, 54.0°, 62.6°, 64.2°, and 71.9°) of α-Fe_2O_3 (JCPDS NO. 33-0664) were also detected over the 10Fe/γ-Al_2O_3 and 10Fe–15Mn/γ-Al_2O_3. Moreover, peaks located at 37.3°, 42.7°, and 56.7° corresponding to MnO_2 (JCPDS NO. 30-0820) were also formed on the surface of the 10Fe–15Mn/γ-Al_2O_3, inferring that the crystal structure of Mn-based oxide changed after the Fe introduction. Compared with the 15Mn/γ-Al_2O_3, the intensities of the Mn diffraction peaks were decreased after the Fe introduction, indicating that Fe and Mn species on the

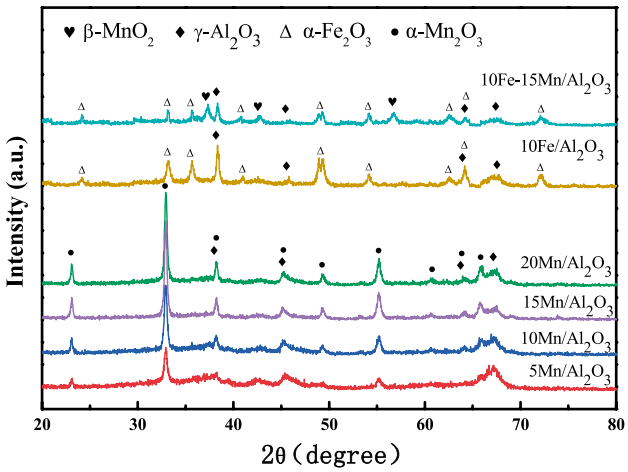

Fig. 1 The X-ray diffraction patterns of the catalysts

Table 1 The BET surface area, pore volume and pore size of catalysts

Catalysts	Surface area (m^2 g^{-1})[a]	Pore volume (cm^3 g^{-1})[b]	Pore diameter (nm)
γ-Al_2O_3	136 ± 9	0.194 ± 0.016	56.75 ± 1.23
3Mn/γ-Al_2O_3	130 ± 6	0.224 ± 0.011	68.60 ± 1.03
5Mn/γ-Al_2O_3	129 ± 7	0.225 ± 0.015	69.60 ± 0.93
10Mn/γ-Al_2O_3	120 ± 8	0.225 ± 0.011	69.60 ± 0.89
15Mn/γ-Al_2O_3	98 ± 6	0.188 ± 0.010	76.78 ± 1.03
20Mn/γ-Al_2O_3	88 ± 3	0.161 ± 0.009	73.20 ± 1.10
10Fe/γ-Al_2O_3	122 ± 7	0.207 ± 0.011	67.95 ± 0.96
10Fe–15Mn/γ-Al_2O_3	106 ± 9	0.176 ± 0.010	66.16 ± 0.93

[a]Surface area was calculated using the BET method at P/P0 = 0.05–0.3

[b]Total pore volume at $P/P_0 = 0.995$

surface of γ-Al_2O_3 were amorphous [17]. The introduction of Fe resulted in a higher distribution of Mn over the surface of the 10Fe–15Mn/γ-Al_2O_3 catalyst. Therefore, interaction between Fe and Mn contributed to the homogeneous distribution of Fe and Mn and suppressed the crystallization of Fe and Mn. The better distribution and amorphous of Fe and Mn in the catalysts exhibited a higher toluene oxidation activity, which was also confirmed by the toluene oxidation activities.

3.1.3 H_2-TPR

In this study, H_2-TPR experiment was carried out to study the redox performance of these Fe–Mn/γ-Al_2O_3 catalysts, as presented in Fig. 2. Previous studies reported that the reduction of Fe_2O_3 to Fe_3O_4 happened at 400 °C, the reduction Fe_3O_4 to FeO took place at 660 °C, and FeO was reduced to form Fe° occurred at 760 °C [38]. As for the MnO_2, the reduction of MnO_2 to Mn_2O_3 took place at 339 °C, Mn_2O_3 to Mn_3O_4 at 472 °C and Mn_3O_4 to MnO at 607 °C [40]. With respect to the 10Fe/γ-Al_2O_3, there were two broad peaks range of 300–450 °C and 500–650 °C (located at 350 °C and 530 °C) observed. The reduction peak at 350 °C was assigned to the reduction of Fe_2O_3 to Fe_3O_4, and the other peak at 530 °C represented the reduction of Fe_3O_4 to FeO since the FeO was stabilized on Al_2O_3 support and the strong interaction between Fe and Al_2O_3 inhibited the transformation of FeO to Fe. For the 15Mn/γ-Al_2O_3, there were only two peaks found. The first peak (happened at 300–400 °C, peak at 375 °C) was attributed to the reduction of MnO_2 to Mn_2O_3; the other peak (occurred at 400–460 °C, peak at 446 °C) was corresponding to the reduction of Mn_2O_3 to Mn_3O_4. With respect to the 10Fe–15Mn/γ-Al_2O_3, there were four peaks observed. The first stage (occurs at 200–340 °C, peak at 310 °C) was attributed to the reduction of MnO_2 to Mn_2O_3. The second stage (happened at 340–400 °C, peak at 380 °C) was mainly assigned to the reduction of Fe_2O_3 to Fe_3O_4. The third stage with temperature range of 400–500 °C belongded to the reduction of Mn_2O_3 to Mn_3O_4. The last stage (500–850 °C) was likely originated from the reduction of Fe_3O_4 to FeO, FeO to Fe° and Mn_3O_4 to MnO.

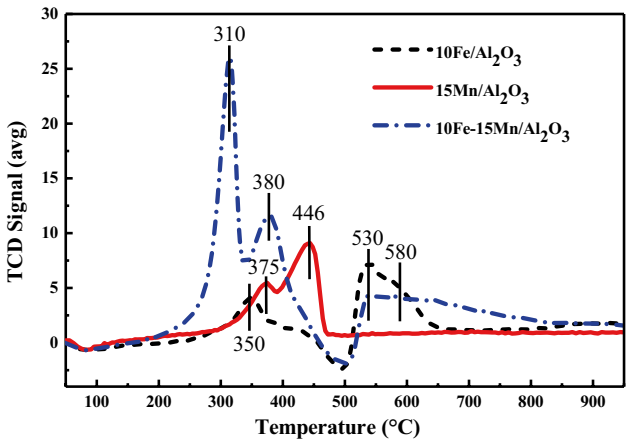

Fig. 2 H_2-TPR profiles of the catalysts

According to the calculation, the theoretical H_2 consumption were in sequence as 331, 354 and 604 μmol g^{-1} for the 15Mn/γ-Al_2O_3, 10Fe/γ-Al_2O_3 and 10Fe–15Mn/γ-Al_2O_3. However, the H_2 consumption results of H_2-TPR exhibited that the reduction of the 10Fe–15Mn/γ-Al_2O_3 (513 μmol g^{-1}) consumed much more H_2 than that of the 15Mn/γ-Al_2O_3 (254 μmol g^{-1}) and the 10Fe/γ-Al_2O_3 (278 μmol g^{-1}), indicated that more oxygen species in the 10Fe–15Mn/γ-Al_2O_3, as shown in Table 2. The above value inferred that the reduction extent of 15Mn/γ-Al_2O_3, 10Fe/γ-Al_2O_3 and 10Fe–15Mn/γ-Al_2O_3 were 76.74%, 78.53%, and 84.93%, respectively. It also can be seen from the H_2-TPR curves that the reduction peaks were shifted to a lower temperature, indicating that the 10Fe–15Mn/γ-Al_2O_3 was more easily reduced by H_2 with respect to the 10Fe/γ-Al_2O_3 and 15Mn/γ-Al_2O_3. The above phenomena can be explained that more active component migrates from the bulk to the surface of the 10Fe–15Mn/γ-Al_2O_3 catalyst [37], which is also confirmed by the ICP/MS results that the Mn concentration on the surface of catalyst increases from 1.82 to 2.01% after the introduction of 10% Fe_2O_3 into the 15Mn/γ-Al_2O_3 catalyst, as shown in Table 2.

3.1.4 XPS

XPS was employed to analyze the elemental composition of these Fe–Mn/γ-Al_2O_3 catalysts, as displayed in Fig. 3 and Table 2. In the survey spectrum, four main peaks attributing to the binding energies of Al (2p), O(1s), Fe(2p) and Mn(2p) were observed in the 10Fe–15Mn/γ-Al_2O_3, as noted in Fig. 3a. Figure 3b indicated that two main bands corresponding to the Mn 2p3/2 and Mn 2p1/2 were found from 638 to 658 eV in the Mn 2p XPS spectra. Meanwhile, the Mn 2p3/2 spectra of these catalysts by a peak-fitting treatment were divided into two peaks, which were attributed to Mn^{4+} and Mn^{3+} in these catalyst. The binding energies of Mn^{4+} and Mn^{3+} located at the Mn 2p3/2 spectra of these catalysts were observed at about 643.5 and 641.4 eV, respectively. The ratio of $Mn^{3+}/(Mn^{3+}+Mn^{4+})$ was calculated according to the integral area of the Mn 2p peaks, as shown in Table 2. The $Mn^{3+}/(Mn^{3+}+Mn^{4+})$ ratios for the 15Mn/γ-Al_2O_3 and 10Fe–15Mn/γ-Al_2O_3 catalysts are 0.47 and 0.53, respectively. Therefore, the incorporation of Fe into 15Mn/γ-Al_2O_3 increases the $Mn^{3+}/(Mn^{3+}+Mn^{4+})$ ratio and provide a relatively stability on the Fe^{3+} and $Mn^{3+}/(Mn^{3+}+Mn^{4+})$ sites [36].

Figure 3c exhibited the Fe 2p spectra of the 10Fe/γ-Al_2O_3 and 10Fe–15Mn/γ-Al_2O_3 catalysts. The Fe species located

Table 2 Element composition and H_2 conssumption of these catalysts

Catalysis	ICP/MS		XPS[a]			XPS[a]			H_2-TPR	
	Fe (%)	Mn (%)	Fe (%)	Mn (%)	O (%)	$(O_\beta+O_\gamma)/(O_\alpha+O_\beta+O_\gamma)$	$Fe^{3+}/(Fe^{2+}+Fe^{3+})$	$Mn^{3+}/(Mn^{3+}+Mn^{4+})$	Theoretical H_2 consumption (μmol g^{-1})	H_2 consumption (μmol g^{-1})
γ-Al_2O_3	0	0	0	0	60.9	29.16	–	–	–	–
5Mn/γ-Al_2O_3	0	0.86	0	1.42	58.7	7.36	–	46.39	–	–
10Mn/γ-Al_2O_3	0	1.69	0	1.84	57.4	35.17	–	51.02	–	–
15Mn/γ-Al_2O_3	0	1.82	0	2.11	56.5	41.52	–	46.98	331	254
20Mn/γ-Al_2O_3	0	2.10	0	2.42	54.1	46.67	–	50.34	–	–
10Fe/γ-Al_2O_3	1.32	0	1.19	0	55.2	21.75	33.90		354	278
10Fe–15Mn/γ-Al_2O_3	0.89	2.01	1.21	2.31	52.6	76.72	46.98	53.33	604	513

[a]Although the accuracy for element analysis from XPS is limited by some deviation, the results are still competent to distinguish the difference

between 704.0 and 736.0 eV were ascribed to the Fe 2p3/2 and Fe 2p1/2 species. The peaks of Fe 2p3/2 and Fe 2p1/2 for the 10Fe/γ-Al_2O_3 were located at 710.7 and 723.9 eV, respectively, while the peaks of Fe 2p3/2 and Fe 2p1/2 for the 10Fe/γ-Al_2O_3 were located at 711.4 and 722.8 eV. The above results indicated that the Fe^{3+} was abundant in these two catalysts. Table 2 also showed that the Fe concentration in the 10Fe/γ-Al_2O_3 was 1.32%, while the Fe concentration was decreased to 0.89% in the 10Fe–15Mn/γ-Al_2O_3. Compared with the 10Fe/γ-Al_2O_3, the $Fe^{3+}/(Fe^{2+}+Fe^{3+})$ ratio was increased from 33.90 to 46.98% for the 10Fe–15Mn/γ-Al_2O_3. The above results also proved that the interaction effect existed between Fe and Mn during impregnation process, and the incorporation of the Fe caused the Mn to accumulate on the surface of catalysts, which favored to promote the catalytic oxidation reaction. In addition, the abundant of Fe^{3+} and Mn^{3+} over the 10Fe–15Mn/γ-Al_2O_3 catalyst favored for the oxygen transfer in the catalyst.

Figure 3d presented the O 1s spectra of these catalysts. The O 1s spectra of these catalysts can be fitted with two peaks, except for the 10Fe–15Mn/γ-Al_2O_3. The binding energy at 529.6–529.7 eV was assigned to the surface lattice oxygen (O_α), while the binding energy at 531.0–531.1 eV was attributed to the surface adsorbed oxygen (O_β). Compared with the 15Mn/γ-Al_2O_3, the binding energies of O_α and O_β in the 10Fe–15Mn/γ-Al_2O_3 were shifted to the low values (O_α 0.5 eV, O_β 1.0 eV), indicating that the O species in the 10Fe–15Mn/γ-Al_2O_3 was more active that was more beneficial to the toluene oxidation [37]. Meanwhile, only the 10Fe–15Mn/γ-Al_2O_3 exhibited a peak at 531.8 eV that may be corresponding to the adsorbed molecular water species (O_γ), which may result in higher water resistance for the 10Fe–15Mn/γ-Al_2O_3. The $(O_\beta+O_\gamma)/(O_\alpha+O_\beta+O_\gamma)$ ratio for the 15Mn/γ-Al_2O_3 was 41.52%, while the $(O_\beta+O_\gamma)/(O_\alpha+O_\beta+O_\gamma)$ ratio for the 10Fe–15Mn/γ-Al_2O_3 was 76.72%. The above results indicated that the 10Fe–15Mn/γ-Al_2O_3 contained higher contents of O_β and O_γ. The higher content of the O_β was normally thought to be important for catalytic activity, while the higher content of O_γ was benefitable for water resistance [17]. This was also proved by the experimental results, as presented in Figs. 5 and 6.

3.2 Catalytic Oxidation Activity

The effects of Mn-loading γ-Al_2O_3 or Fe-loading γ-Al_2O_3 on the toluene conversion under different reaction temperatures were presented in Fig. 4. As noted in Fig. 4a, the toluene conversions over the Mn/γ-Al_2O_3 catalysts were all increased as the reaction temperature increased from 100 to 400 °C. After 5–20% of MnO_2 doping into the pure γ-Al_2O_3, the toluene conversions under various temperatures were higher than that of the pure MnO_2. Figure 4a also represented that the toluene conversion increased as the MnO_2 loading

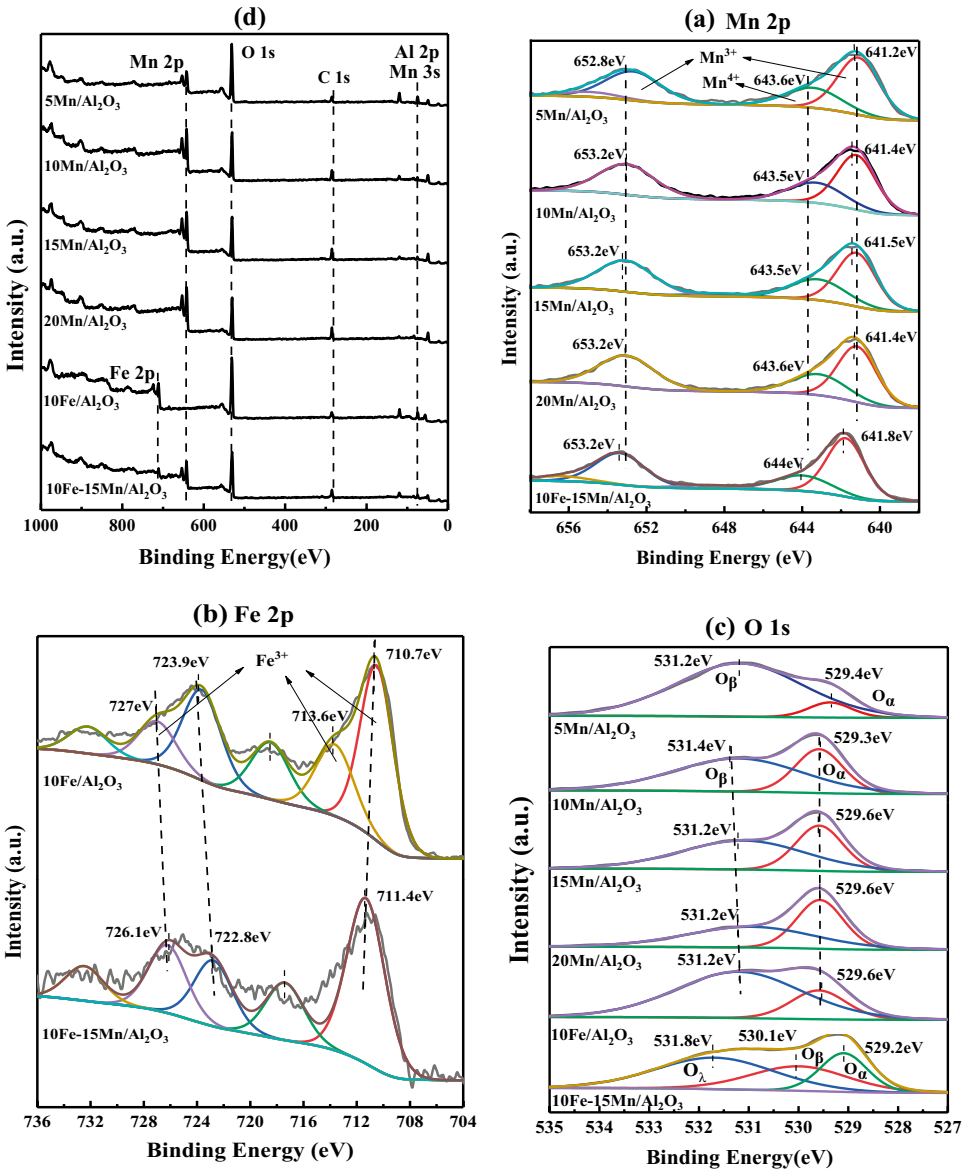

Fig. 3 XPS profiles of catalysts: **a** survey; **b** Mn-2p3/2 orbital; **c** Fe-2p3/2 orbital; **d** O-1 s orbital

was increased from 0 to 15%, while the toluene oxidation activity were not increased as the MnO_2 loading was further increased from 15 to 20%. Meanwhile, more than 80% of the toluene conversion over the 15Mn/γ-Al_2O_3 catalyst could be obtained at 200–400 °C, and the toluene conversion was as high as 92.11% at 300 °C, further increase of temperature can't obviously enhance the toluene conversion. Therefore, the optimal temperature was 300 °C and the best MnO_2-loading is 15%. The effect of Fe_2O_3-loading γ-Al_2O_3 on the toluene conversion at different reaction temperatures were represented in Fig. 4b. Similar with the Mn/γ-Al_2O_3 catalyst, the toluene conversions under various temperatures were increased as the Fe_2O_3-loading was increased from 3 to 15%, further increase of Fe_2O_3-loading also can't increase the activity, and the maximum toluene conversion of 46.25% over the 15Fe/γ-Al_2O_3 catalyst was obtained at 400 °C. Moreover, the effects of GHSV, O_2 content and H_2O content on the toluene oxidation performance were investigated over the 15Mn/γ-Al_2O_3 and 15Fe/γ-Al_2O_3 catalysts, as shown in Fig. S1–Fig. S3. The results indicated that the toluene conversion decreased as the GHSV was increased from 10,000 to 30,000 h^{-1} under various temperature. Meanwhile, the toluene conversion increased as the O_2 content was increased from 3 to 10%, while further increased of the O_2 content can't increase the toluene conversion. Fig. S3 indicated the toluene conversion over the 15Mn/γ-Al_2O_3 catalyst gradually decreased from 92.31 to 84.58% for 6 h, and the CO_2 yield reduced from 92 to 76% when the 10 vol% of water was introduced, indicating that the 15Mn/γ-Al_2O_3 displayed a higher catalytic activity, and it should be modified to enhance the moisture toleration. The toluene oxidation consumed oxygen and released H_2O and CO_2, and

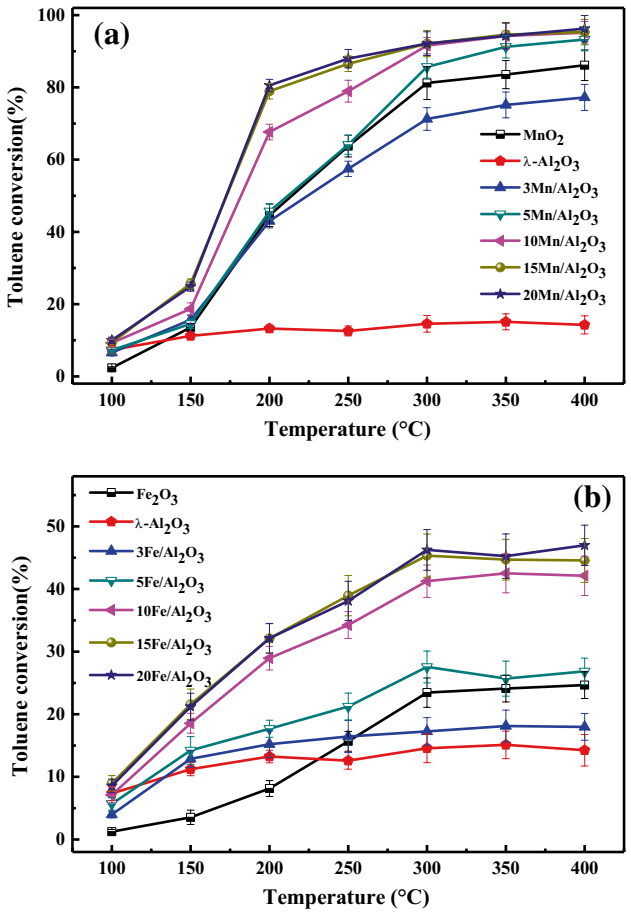

Fig. 4 The effects of Mn-loading γ-Al_2O_3 or Fe-loading γ-Al_2O_3 on toluene conversion

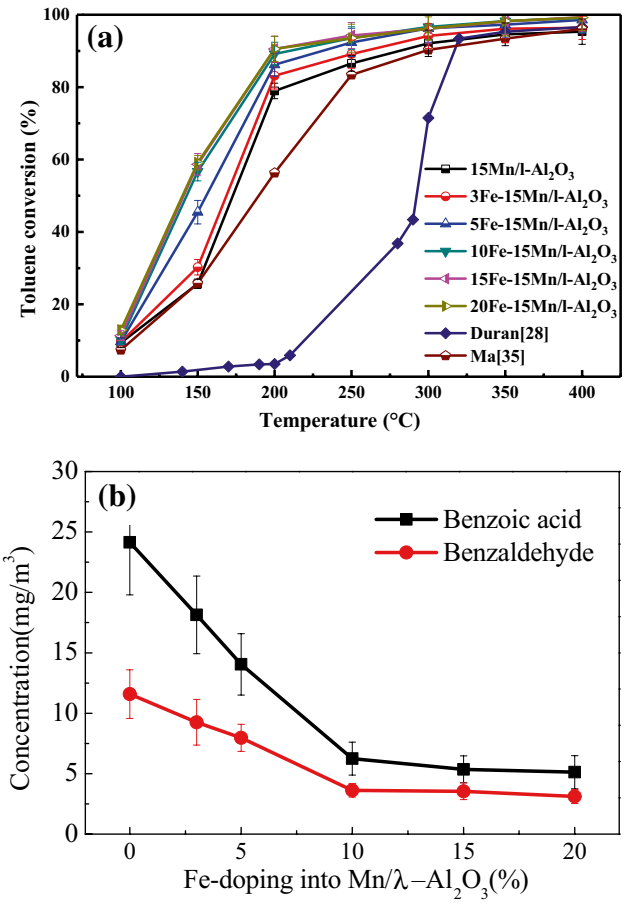

Fig. 5 Effect of Fe-doping into 15Mn/γ-Al_2O_3 catalyst on the toluene conversion and byproducts formation

the reaction followed toluene → benzaldehyde → benzoic acid → $H_2O + CO_2$ steps [22]. According to the reaction, the presence of the H_2O was unfavorable for the reactions [17]. Therefore, the introduction of H_2O had negative influence on the CO_2 yield as well as the toluene oxidation efficiency. However, the toluene conversion over the 10Fe/γ-Al_2O_3 stabled at 31.5% and the CO_2 yield was 85% in presence of 10 vol% H_2O at 300 °C, inferring that the Fe/γ-Al_2O_3 exhibited an excellent moisture toleration but lower catalytic activity.

To enhance the VOCs oxidation performance (higher catalytic activity as well as excellent moisture toleration), the introduction of Fe_2O_3 into Mn/γ-Al_2O_3 to prepare Fe–Mn/γ-Al_2O_3 catalyst were investigated. Figure 5 displayed the effect of Fe_2O_3-doping into 15Mn/γ-Al_2O_3 catalyst on the toluene conversion. The results indicated that the toluene conversion over the xFe–15Mn/γ-Al_2O_3 at 100–400 °C obviously increased as the Fe-doping was increased from 0 to 10%, while the toluene conversion varied slightly with the Fe-doping further increased. It could be seen that 89.15% and 96.62% of toluene conversion over the 10Fe–15Mn/γ-Al_2O_3 were obtained at 200 °C and 300 °C, indicating that

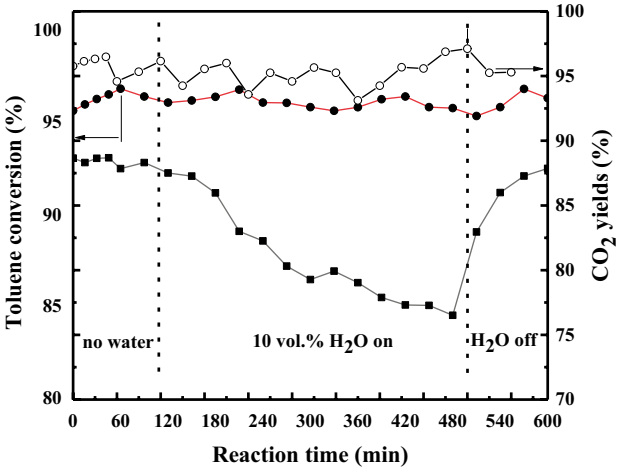

Fig. 6 Effect of water vapor on catalytic performance of 10Fe–15Mn/γ-Al_2O_3 catalyst

the toluene oxidation activity over the 10Fe–15Mn/γ-Al_2O_3 was much better than that obtained from Duran [28] and Ma [35]. Meanwhile, Fig. 5b also indicated that the byproducts such as benzaldehyde and benzoic acid were also detected by the GC/MS at 300 °C, and their contents were decreased with the Fe-doping. In order to further examine the moisture toleration of the 10Fe–15Mn/γ-Al_2O_3 catalyst, the effect of H_2O on the toluene oxidation of the 10Fe–15Mn/γ-Al_2O_3 was investigated under the GHSV of 20,000 h^{-1} with 10 vol% H_2O at 300 °C, as shown in Fig. 6. The result indicated 95% of the toluene conversion as well as 95% CO_2 yield over the 10Fe–15Mn/γ-Al_2O_3 sustained for 6 h under the GHSV of 20,000 h^{-1} with 10 vol% H_2O at 300 °C. Therefore, the 10Fe–15Mn/γ-Al_2O_3 catalyst showed a good catalytic activity as well as excellent moisture toleration. There were three reasons caused the above results: Firstly, the introduction of Fe into 15Mn/γ-Al_2O_3 resulted in the formation of Fe–OH due to the combination of Fe^{3+} and –OH, which can not only improves water resistance, but also drives electron transfer in redox process [37]. Secondly, the change of iron valence ($Fe^{3+} \Leftrightarrow Fe^{2+} \Leftrightarrow Fe$) was benefitable for the storing and releasing oxygen [17]. Lastly, the introduction of Fe into 15Mn/γ-Al_2O_3 caused Mn to accumulate and homogeneous distribution on the surface of catalysts, which promoted the oxidation reaction and enhanced the toluene conversion [41], as confirmed by XPS and XRD.

3.3 Mechanism for Catalytic Oxidation of Toluene

The absorption and activation are two main steps for the toluene oxidation reaction [42]. Therefore, the absorption and oxidation over the Mn/γ-Al_2O_3 catalysts were performed to analyze the transformation of intermediates during the toluene oxidation process. In this study, toluene absorption over these catalysts was carried out at 300 °C in Ar atmosphere, while toluene oxidation was carried out in presence of O_2. The toluene absorption and oxidation over Mn/γ-Al_2O_3 catalysts at 300 °C were presented in Fig. 7a and b. As noted in Fig. 7a, the peak centered at 1600 cm^{-1} was derived from vibration of aromatic ring, indicating the toluene was adsorbed over the catalysts and its aromatic structure keep intact [17]. Two peaks located at 2885 and 3019 cm^{-1} were observed in the C–H stretching region. One band at 3019 cm^{-1} was assigned to the C–H stretching in aromatic rings, and another band at 2885 cm^{-1} was attributed to C–H symmetric or asymmetric stretching of methylene (–CH_2) [22]. The bands appeared at 1160 cm^{-1} belonged to the C–O vibration, which was caused by the formation of alkoxide specie [43]. Meanwhile, the peak corresponding to alkoxide specie was also detected at 3423 cm^{-1}, which directly reflected the formation of phenyl alcohol [34]. However, Du et al. [22] claimed that the peak at 1159 cm^{-1} was assigned to the C–O vibration from the phenolate. Peaks at

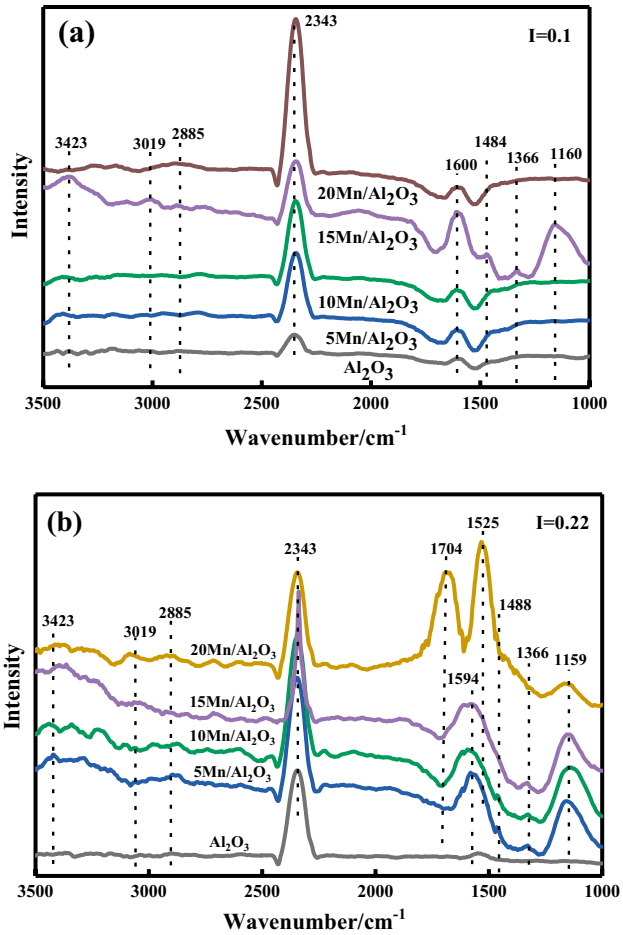

Fig. 7 The profiles of toluene desorption and oxidation over Mn/γ-Al_2O_3 catalysts: **a** Ar atmosphere; **b** O_2/Ar atmosphere

1366 cm^{-1} and 1484 cm^{-1} belonged to carboxylate, suggesting benzoate species was a key intermediates during toluene oxidation process [22]. Figure 7a also represented that the 15Mn/γ-Al_2O_3 exhibited the highest peaks of adsorbed toluene (1600 cm^{-1}), alkoxide specie (3423 cm^{-1}) and carboxylate (1366 cm^{-1} and 1484 cm^{-1}) among all the Mn/γ-Al_2O_3 catalysts, indicating that the toluene was more easily adsorbed over the 15Mn/γ-Al_2O_3, and alkoxide and carboxylate species were the main intermediates in the absence of O_2 [41]. Peak at 2349 cm^{-1} was assigned to the CO_2, indicating CO_2 can be formed without O_2 [44]. Figure 7b presented the in situ DRIFT spectra of the toluene oxidation over these catalysts in presence of O_2. Compared with the spectra obtained without O_2, some obvious changes were found in presence of O_2: (1) The peaks for aldehydic species (peak at 1704 cm^{-1}) and carboxylate (peak at 1525 cm^{-1}) appeared in presence of O_2 when the Mn-doping was above 5%; (2) The bands for aldehydic species (peak at 1704 cm^{-1}) and carboxylate (peak at 1525 cm^{-1}) over the 20Mn/γ-Al_2O_3 were much higher than other catalysts, while the peak located at 1594 cm^{-1}

for toluene absorption disappeared over the 20Mn/γ-Al_2O_3, suggesting that the adsorbed toluene was easily converted into other intermediates over the 20Mn/γ-Al_2O_3 in presence of O_2 with respect to the other Mn/γ-Al_2O_3; (3) The peaks belong to CO_2 (2343 cm^{-1}), aldehydic species (1704 cm^{-1}) and C–O vibration (1160 cm^{-1}) in presence of O_2 were much higher than that obtained from Ar atmosphere, indicating that the intermediates and CO_2 from the toluene oxidation were significantly promoted due to the presence of O_2. The above results demonstrated that the gas-phase oxygen had an greatly influence on the intermediates formation over the Mn/γ-Al_2O_3.

The in situ DRIFT were used to investigate the absorption and oxidation of toluene over the 15Mn/γ-Al_2O_3 at 200–400 °C. As noted in Fig. 8a, the peaks corresponding to the adsorbed toluene (1599 cm^{-1}) and C–O vibration (3424 and 1159 cm^{-1}) are firstly increased and then decreased at 200–400 °C, and the maximum peak obtained at 300 °C, indicating adsorbed toluene was converted into other species with the temperature increase.

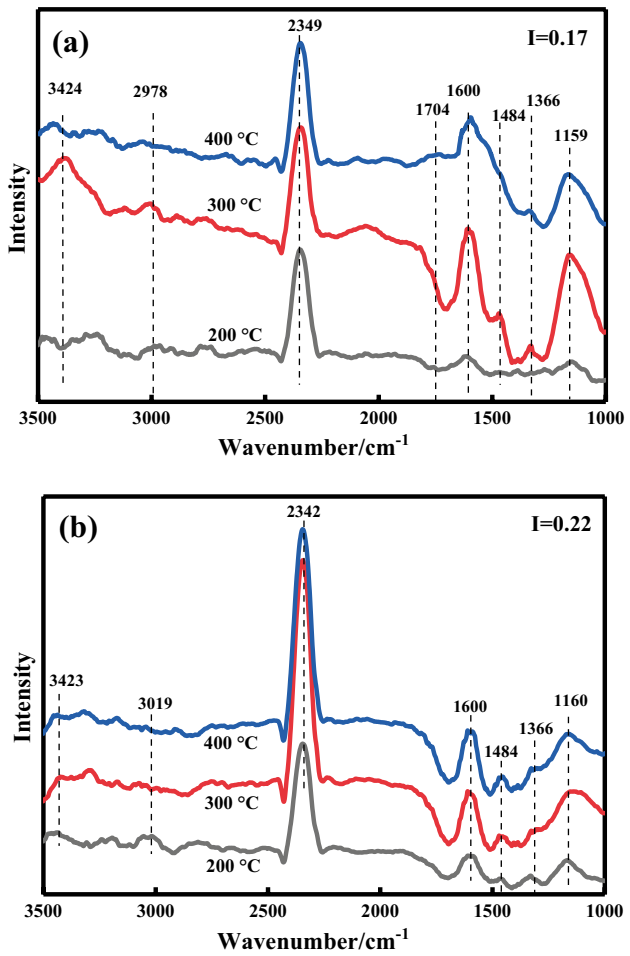

Fig. 8 The in situ DRIFT over 15Mn/γ-Al_2O_3 at 200–400 °C: **a** Ar atmosphere; **b** O_2/Ar atmosphere

Peak at 1704 cm^{-1} corresponding to aldehydic species was observed at 400 °C, indicating the higher temperature was benefitable for the formation of aldehydic species in absence of O_2. The carboxylate (located at 1484 and 1366 cm^{-1}) were increased with the temperature. Meanwhile, the maximum peak of alkoxide specie (at 1160 cm^{-1}) was also obtained at 300 °C. Peak at 2349 m^{-1} associated with CO_2 were increased as the temperature varied from 200 to 400 °C. The above results implied that the higher temperature was benefitable for the toluene absorption over the 15Mn/γ-Al_2O_3, which was consistent with the results obtained from Fig. 4. The in situ DRIFT over the 15Mn/γ-Al_2O_3 for the toluene oxidation at 200–400 °C was represented in Fig. 8b. It was worthy noted that the peaks belong to CO_2 (2349 m^{-1}), adsorbed toluene (1600 cm^{-1}) and C–O vibration (1160 and 3423 cm^{-1}) in presence of O_2 were increased when the temperature was increased from 200 to 300 °C, while there was no obvious change as the temperature was further increased to 400 °C. Meanwhile, peak at 1704 cm^{-1} belonged to the C=O were not observed in presence of O_2, indicating the aldehydic species was easily oxidized into other species (1366 cm^{-1} and 1484 cm^{-1}) in presence of O_2 at 200–400 °C.

In order to evaluate the effect of the Fe-doping into the 15Mn/γ-Al_2O_3 on the toluene absorption and oxidation. The in situ DRIFT over the 15Mn/γ-Al_2O_3, 10Fe/γ-Al_2O_3 and 10Fe–15Mn/γ-Al_2O_3 for the toluene absorption and oxidation at 300 °C were also compared, as shown in Fig. 9. Figure 9 indicated that the peaks for CO_2 (2343 cm^{-1}), aldehydic (1699 cm^{-1}) and carboxylate (at 1519 cm^{-1}) over the 10Fe–15Mn/γ-Al_2O_3 were higher than that obtained from the 15Mn/γ-Al_2O_3 and 10Fe/γ-Al_2O_3, while the adsorbed toluene (1600 cm^{-1}) and C–O vibration (1160 cm^{-1}) over the 10Fe–15Mn/γ-Al_2O_3 disappeared with respect to the 15Mn/γ-Al_2O_3 and 10Fe/γ-Al_2O_3, indicating that the 10Fe–15Mn/γ-Al_2O_3 possessed the best catalytic activity among these catalysts, which was more easily oxidized the adsorbed toluene and alkoxide specie into benzoic acid, CO_2 and H_2O [45, 46], which was in accordance with the result of Fig. 5. Compared with the spectra obtained without oxygen, the peaks for CO_2 (at 2343 cm^{-1}), C=O (at 1704 cm^{-1}) and carboxylate (at 1525 cm^{-1}) over the 10Fe–15Mn/γ-Al_2O_3 in presence of O_2 were much higher, implying that the rate of the oxidation reaction was enhanced by the existence of O_2. The above results indicated that the toluene, benzyl alcohol, and benzoic acid were the main intermediates that could be directly converted into CO_2 in the whole oxidation process. Liao et al. [47] also found that the benzyl alcohol, benzaldehyde and benzoic were the main intermediates during toluene oxidation process. A similar results were also obtained by Du et al. [22] and Sun et al. [43].

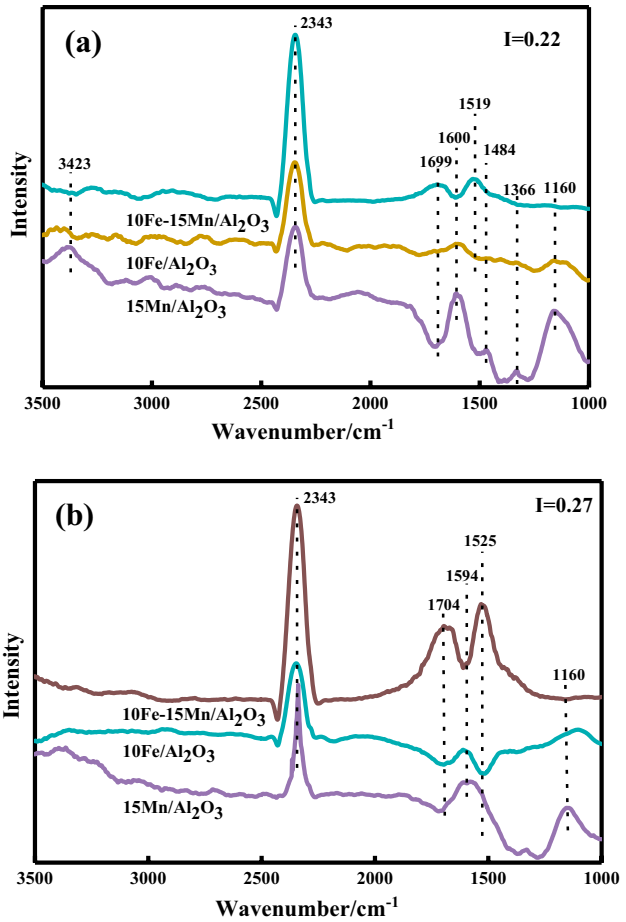

Fig. 9 The in situ DRIFT spectra over 15Mn/γ-Al_2O_3, 10Fe/γ-Al_2O_3 and 10Fe–15Mn/γ-Al_2O_3 catalysts for the toulene adsorption and oxidation at 300 °C: **a** Ar atmosphere; **b** O_2/Ar atmosphere

4 Conclusions

In this study, the Fe-modified Al_2O_3-supported Mn mixed oxide (Fe–Mn/Al_2O_3) catalysts are prepared using the wet-impregnation method. These catalysts are characterized by means of the XRD, BET, XPS, H_2-TPR, and in situ DRIFTS. Meanwhile, the catalytic activities and its mechanism over Fe–Mn/γ-Al_2O_3 catalysts for toluene oxidation are also investigated. The following conclusions have been drawn:

(1) The 10Fe–15Mn/γ-Al_2O_3 exhibited 95% of toluene conversion and 95% of CO_2 yield as well as good stability and higher moisture toleration at 300 °C.
(2) The introduction of Fe into Mn/γ-Al_2O_3 resulted in higher surface area, higher amount of Mn^{4+}/Mn^{3+} and better low-temperature reducibility, as well as homogenous distribution of Mn and Fe.
(3) The Fe–Mn/γ-Al_2O_3 showed a better toluene oxidation performance with respect to the Fe/γ-Al_2O_3 and Mn/γ-Al_2O_3.
(4) The adsorbed toluene over the 10Fe–15Mn/γ-Al_2O_3 could be oxidized to benzyl alcohol that further oxidized to benzoic acid, and then the benzoic acid was decomposed into CO_2 and H_2O.

Acknowledgements This work was supported by the Technology Innovation Special Foundation of Hubei Province (Grant Nos. 2019ACA157, 2019AHB073 and 2019ZYYD060), China Postdoctoral Science Foundation (2018M642960), and Foundation for Outstanding Youth Innovative Research Groups of Higher Education Institution in Hubei Province (T201902).

References

1. Kamal MS, Razzak SA, Hossain MM (2016) Atmos Environ 140:117–134
2. Kansal A (2009) J Hazard Mater 166:17–26
3. Xu M, Yu D, Yao H, Liu X, Qiao Y (2011) Proc Combust Inst 33:1681–1697
4. Chen J, Chen X, Chen X, Xu W, Xu Z, Jia H, Chen J (2018) Appl Catal B 224:825–835
5. Zhang S, You J, Kennes C, Cheng Z, Ye J, Chen D, Chen J, Wang L (2018) Chem Eng J 334:2625–2637
6. Han J, Liang Y, Hu J, Qin L, Street J, Lu Y, Yu F (2017) Energy Convers Manag 153:641–648
7. Han J, Zhang L, Kim HJ, Kasadani Y, Li L, Shimizu T (2018) Fuel Process Technol 176:15–20
8. Zhang Q, Wu L, Fang X, Liu M, Zhang J, Shao M, Lu S, Mao H (2018) Sci Total Environ 624:878–886
9. Zhang X, Gao B, Creamer AE, Cao C, Li Y (2017) J Hazard Mater 338:102–123
10. Dai C, Zhou Y, Peng H, Huang S, Qin P, Zhang J, Yang Y, Luo L, Zhang X (2018) J Ind Eng Chem 62:106–119
11. Qin L, Han J, Zhan Y, Chen W, Kim H (2016) Energy Fuels 30:544–550
12. Qin L, Han J, Zhao B, Chen W, Xing F (2018) Waste Manag Res 36:1073–1082
13. Qin L, Han J, Zhao B, Wang Y, Chen W, Xing F (2018) J Anal Appl Pyrol 136:132–145
14. Qin L, Xing F, Zhao B, Chen W, Han J (2018) Chemosphere 212:200–208
15. Mustafa MF, Fu X, Liu Y, Abbas Y, Wang H, Lu W (2018) J Hazard Mater 347:317–324
16. Shayegan Z, Lee C-S, Haghighat F (2018) Chem Eng J 334:2408–2439
17. Chen J, Chen X, Xu W, Xu Z, Chen J, Jia H, Chen J (2017) Chem Eng J 330:281–293
18. Mirzaei A, Leonardi SG, Neri G (2016) Ceram Int 42:15119–15141
19. Du C, Lu S, Wang Q, Buekens AG, Ni M, Debecker DP (2018) Chem Eng J 334:519–544
20. Castaño MH, Molina R, Moreno S (2017) Mol Catal 443:117–124
21. Ren K, Song J, Song Y-H, Wang H, Liu Z, Liu Z-T, Jiang J, Liu Z-W (2017) J CO2 Util 22:63–70
22. Du J, Qu Z, Dong C, Song L, Qin Y, Huang N (2018) Appl Surf Sci 433:1025–1035
23. Zhang X, Junhui Y, Jing Y, Ting C, Bei X, Zhe L, Kunfeng Z, Ling Y, Dannong H (2018) Appl Catal A 566:104–112
24. Wang Y, Yang D, Li S, Zhang L, Zheng G, Guo L (2019) Chem Eng J 357:258–268
25. Hu J, Li WB, Liu RF (2018) Catal Today 314:147–153

26. Tang A, Hu L, Yang X, Jia Y, Zhang Y (2016) Catal Commun 82:41–45
27. Baldi M, Escribano VS, Amores JMG, Milella F, Busca G (1998) Appl Catal B Environ 17:175–182
28. Durán FG, Barbero BP, Cadús LE, Rojas C, Centeno MA, Odriozola JA (2009) Appl Catal B 92:194–201
29. Quiroga MMB, Barbero BP, Cadus LE (2014) Appl Catal A 474:26–33
30. Castaño MH, Molina R, Moreno S (2015) Appl Catal A 492:48–59
31. Pozan GS (2012) J Hazard Mater 221–222:124–130
32. Esmaeilirad M, Zabihi M, Shayegan J, Khorasheh F (2017) J Hazard Mater 333:293–307
33. Shu Y, Xu Y, Huang H, Ji J, Liang S, Wu M, Leung DYC (2018) Chemosphere 208:550–558
34. Wang H, Lu Y, Han Y, Lu C, Wan H, Xu Z, Zheng S (2017) Appl Surf Sci 420:260–266
35. Ma WJ, Huang Q, Xu Y, Chen YW, Zhu SM, Shen SB (2013) Ceram Int 39:277–281
36. Chen C, Li Y, Ma W, Guo S, Wang Q, Li QX (2017) Sep Purif Technol 183:1–10
37. Wang X, Wu S, Zou W, Yu S, Gui K, Dong L (2016) Chin J Catal 37:1314–1323
38. Chen W, Li Z, Hu F, Qin L, Han J, Wu G (2018) Appl Surf Sci 439:75–81
39. Chen W, Luo J, Qin L, Han J (2015) J Environ Manag 164:146–150
40. Cao F, Su S, Xiang J, Wang P, Hu S, Sun L, Zhang A (2015) Fuel 139:232–239
41. Luo Y, Zheng Y, Zuo J, Feng X, Wang X, Zhang T, Zhang K, Jiang L (2018) J Hazard Mater 349:119–127
42. Farmanzadeh D, Valipour A (2018) Appl Surf Sci 450:509–515
43. Sun H, Liu Z, Chen S, Quan X (2015) Chem Eng J 270:58–65
44. Long Y, Wu S, Xiao Y, Cui P, Zhou H (2018) J Clean Prod 181:784–793
45. Han J, Liang Y, Qin L, Zhao B, Wang H, Wang Y (2019) Catal Lett 149:3224–3237
46. Wang H, Han J, Bo Z, Qin L, Wang Y, Yu F (2019) Mol Catal 475:110486
47. Liao Y, Zhang X, Peng R, Zhao M, Ye D (2017) Appl Surf Sci 405:20–28

Publisher's Note Springer Nature remains neutral with regard to jurisdictional claims in published maps and institutional affiliations.